Plasma Chem Plasma Process (2011) 31:1–21
DOI 10.1007/s11090-010-9275-y

ORIGINAL PAPER

Investigation of the Atmospheric Helium Dielectric Barrier Discharge Driven by a Realistic Distorted-Sinusoidal Voltage Power Source

C.-T. Hung · Y.-M. Chiu · F.-N. Hwang · M.-H. Chiang · J.-S. Wu · Y.-C. Wang

Received: 29 April 2010 / Accepted: 14 October 2010 / Published online: 18 November 2010

Abstract The non-equilibrium atmospheric-pressure parallel-plate helium dielectric barrier discharge (DBD) driven by a realistic 20 kHz distorted-sinusoidal voltage waveform has been investigated by means of simulations and experiments. A self-consistent one-dimensional fluid modeling code considering the non-local electron energy balance was applied to simulate the helium DBD. The effect of selecting plasma chemistry was investigated by comparing simulations with experiments. The results show that the simulations, which include more excited helium, metastable helium and electron–ion-related reaction channels, can faithfully reproduce the measured discharged temporal current quantitatively. Based on the simulated discharge properties, we have found that there is complicated mode transition of discharges from the long Townsend-like to the "dark current"-like, then to the short primary Townsend-like and the short secondary Townsend-like for the helium DBD that is driven by a realistic distorted-sinusoidal voltage power source. Discharge properties in different periods of discharge are discussed in detail in the paper.

Keywords Townsend-like discharge · Atmospheric pressure plasmas · Helium · Fluid modelling · Dielectric barrier discharge

Introduction

Atmospheric-pressure plasmas (APP) have attracted a tremendous amount of attention in the past two decades, mainly because: (1) they do not require the use of vacuum equipment and (2) they have increasingly numerous applications in modern science and technology. The former drives the cost down dramatically compared with those that have been used in materials processing and also offers the possibility of in-line processing in industry. The latter may include surface cleaning [1], surface modification [2], thin film deposition [3],

C.-T. Hung · Y.-M. Chiu · M.-H. Chiang · J.-S. Wu (✉) · Y.-C. Wang
Department of Mechanical Engineering, National Chiao Tung University, Hsinchu, Taiwan
e-mail: chongsin@faculty.nctu.edu.tw

F.-N. Hwang
Department of Mathematics, National Central University, Chung-Li, Taiwan

etching [4], biological decontamination [5], ozone generation [6], pollution control [7], flat plasma display panels [8] and gas lasers [9], to name a few.

The types of APP are generally classified based on the power sources, which may include radio frequency (RF) capacitively coupled discharge, alternating current (AC) dielectric barrier discharge (DBD) and microwave discharge. Among these, helium DBD may represent one of the most popular discharges because of its easier implementation and numerous applications. In addition to experimental diagnostics, fluid modeling has been proved to be a very useful tool for understanding the plasma physics and chemistry of helium discharges. Indeed, the outcome of fluid modeling strongly depends on the selection of the plasma chemistry and other parameters such as transport coefficients and rate constants, in addition to the numerical accuracy of the simulation itself. Thus, in this paper we intend to present the effect of selecting simple and complicated plasma chemistry on simulating helium DBD driven by a realistic bipolar pulsed power supply using fluid modeling by comparisons with experimental data and to elucidate the underlying physics based on the simulation data.

In the literature, there are many fluid modeling studies on the topic of helium DBD under the atmospheric-pressure condition as described in the following.

On one hand, in the case of RF AP discharge, one-dimensional fluid modeling was often used to elucidate the plasma physics by varying parameters such as the gap distance, the amplitude of the sinusoidal voltage, the frequency of the sinusoidal voltage, the mixture of impurities and the secondary electron emission coefficient [10–14]. In these studies, very simplified helium plasma chemistry was used and generally was in reasonable agreement with experimentally measured discharged currents.

On the other hand, in the case of AC DBD, one-dimensional fluid modeling was also often used by parametric studies to study the discharge physics. These include changes in the gap distance, the dielectric thickness, the dielectric permittivity, the amplitude and frequency of the sinusoidal voltage in the range of 10–130 kHz, the mixture of impurities, the voltage waveform (e.g., pulsed or others) and secondary electron emission, among others [15–21]. In these studies, a relatively complicated helium plasma chemistry set was adopted to simulate the discharge physics. These plasma chemistries generally included more reaction channels related to excited and metastable helium. The results of DBD studies [15–18, 20] generally followed the trends of the experimental data, although quantitative comparison is still not favorable to the best knowledge of the authors. The reason should be attributed to the use of local field approximation (LFA), which assumes that the input electric power into the plasma is balanced with the power consumed by local reactions. It has been confirmed that the use of local mean energy approximation (LMEA) generally leads to better results than LFA because the LMEA considers the non-local effect of electron energy distribution [22]. This may become more important for APPs since the electron-neutral elastic collision becomes non-negligible under the atmospheric condition, which is not considered at all in LFA.

There seems to be no previous study focusing on the detailed comparison of the selection of plasma chemistry in the fluid modeling of helium DBD driven by a realistic distorted-sinusoidal power source and its direct validation by comparisons with the experimental data, although this is important in conducting useful fluid modeling for this type of discharge. Also, there has been no detailed study discussing the detailed mode transition within a cycle for a realistic quasi-pulse power source. Thus, it is the major objective of this current study to present the effect of selecting plasma chemistry in helium DBD simulations driven by a realistic quasi-pulse power source and to compare the simulation quantitatively with the experimental data.

In this study, one-dimensional self-consistent fluid modeling using the fully implicit method was employed to simulate the helium DBD (driven by a distorted-sinusoidal waveform, 20 kHz power source) using simple and complicated plasma chemistry, respectively, and to compare with the experimental discharge currents obtained in the present study. In addition, several temporal and spatial distributions of important properties are presented to explain in detail the effect of selecting helium plasma chemistry. The results show that the inclusion of more excited and metastable species-related channels in the plasma chemistry is critical for predicting the correct discharge currents in the fluid modeling of helium DBD driven by the complicated applied voltage power source.

The remainder of the paper is organized as follows. The numerical method is introduced in Sect. 2, followed by a description of the experimental method in Sect. 3. Then, the detailed results are presented and discussed accordingly. Finally, the major findings of the present study are summarized at the end of the paper.

Numerical Method

Fluid Modeling Equations

In the framework of fluid modeling, electron and ion number densities are calculated as functions of time and space resulting from the coupled solution of the species continuity equation, species momentum equation, species energy equation and field equations. Since the fluid modeling equations are similar for most of the gas discharges, we only summarize a typical set of equations in the following as the model equations for the purpose of demonstration. Note that we neglect flow convection effects in the present study.

The general continuity equation for ion species can be written as

$$\frac{\partial n_p}{\partial t} + \vec{\nabla} \cdot \vec{\Gamma}_p = \sum_{i=1}^{r_p} S_{pi} \quad p = 1, \ldots K \tag{1}$$

where n_p is the number density of ion species p, K is the number of ion species, r_p is the number of reaction channels that involve the creation and destruction of ion species p and $\vec{\Gamma}_p$ is the particle flux that is expressed, based on the drift–diffusion approximation, as

$$\vec{\Gamma}_p = \text{sign}(q_p)\mu_p n_p \vec{E} - D_p \vec{\nabla} n_p \tag{2}$$

$$\vec{E} = -\nabla \varphi \tag{3}$$

where q_p, $\vec{E}$, μ_p, D_p and α_{iz} are the ion charge, the electric field, the electron mobility, the electron diffusivity and the ionization rate, respectively. Note that the form of the source term S_{pi} can be modified according to the modelled reactions describing how the ion species p is generated or destroyed in reaction channel i. The boundary conditions at the walls are applied considering thermal diffusion, drift and diffusion fluxes.

The continuity equation for electron species e can be written as

$$\frac{\partial n_e}{\partial t} + \vec{\nabla} \cdot \vec{\Gamma}_e = \sum_{i=1}^{r_e} S_{e_i} \tag{4}$$

where n_e is the number density of ions, r_e is the number of reaction channels that involve the creation and destruction of electrons and $\vec{\Gamma}_e$ is the corresponding particle flux that is expressed, based on drift–diffusion approximation, as

$$\vec{\Gamma}_e = -\mu_e n_e \vec{E} - D_e \vec{\nabla} n_e \tag{5}$$

where μ_e and D_e are the electron mobility and electron diffusivity, respectively. These two transport coefficients can be readily obtained as a function of the electron temperature from the solution of a publicly available computer code for the Boltzmann equation, named BOLSIG+ [23]. Similar to S_{pi}, the form of S_{e_i} can also be modified according to the modelled reactions that generate or destroy the ion in reaction channel i. The boundary conditions at the walls are applied considering the thermal diffusion, drift and diffusion fluxes of the electrons. Secondary electron emission or photo-electron emission from the solid walls can be readily added if necessary.

The continuity equation for neutral species can be written as

$$\frac{\partial n_{uc}}{\partial t} + \vec{\nabla} \cdot \vec{\Gamma}_{uc} = \sum_{i=1}^{r_{uc}} S_{uc_i} \quad uc = 1, \ldots, L \tag{6}$$

where n_{uc} is the number density of uncharged species uc, L is the number of neutral species, r_{uc} is the number of reaction channels that involve the creation and destruction of uncharged species uc and $\vec{\Gamma}_{uc}$ is the corresponding particle flux, neglecting convection effects, which can be expressed as

$$\vec{\Gamma}_{uc} = -D_{uc} \vec{\nabla} n_{uc} \tag{7}$$

where D_{uc} is the diffusivity of neutral species. Similarly, the form of S_{uc_i} can also be modified according to the modelled reactions that generate or destroy the species in reaction channel i. Neumann boundary conditions at the walls are applied since no surface reactions are considered in the present study.

The electron energy density equation can be expressed as

$$\frac{\partial n_\varepsilon}{\partial t} + \nabla \cdot \vec{\Gamma}_{n_\varepsilon} = -e\vec{\Gamma}_e \cdot \vec{E} - \sum_{i=1}^{S_c} \varepsilon_i S_i + 3\frac{m_e}{M} n_e k_B \nu_m \left(T_e - T_g\right) \tag{8}$$

where $n_\varepsilon \left(= \frac{3}{2} n_e k_B T_e\right)$ is the electron energy density, T_e is the electron temperature, ε_i is the energy loss for the ith inelastic electron collision, k_B is the Boltzmann constant, ν_m is the momentum exchange collision frequency between the electron (mass m_e) and the background neutral (mass M), T_g is the background gas temperature and $\vec{\Gamma}_{n_\varepsilon}$ is the corresponding electron energy density flux as

$$\vec{\Gamma}_{n_\varepsilon} = \frac{5}{2} k_B T_e \vec{\Gamma}_e - \frac{5}{2} \frac{n_e k_B T_e}{m_e \nu_m} \nabla (k_B T_e) \tag{9}$$

The second term on the right-hand side of Eq. 8 represents the sum of the energy losses of the electrons due to inelastic collision with other species. The last term on the right-hand side of Eq. 8 can be ignored for low-pressure gas discharges, while it is important for medium-to-atmospheric pressure discharges. Similarly, the boundary conditions at the walls are applied considering thermal diffusion, drift and diffusion fluxes. Secondary electron emission and other boundary effects can be readily added if needed.

Poisson's equation for electrostatic potential can be expressed as

$$\nabla \cdot (\varepsilon \nabla \varphi) = \left(\sum_{i=1}^{K} q_i n_i - e n_e \right) \tag{10}$$

where φ is the potential and ε is a function of position, whose value is either the vacuum or dielectric permittivity, depending upon the problem. All the transport properties of neutral and ions are obtained from literature data [12, 24].

Discretization, Numerical Schemes and Algorithms

In the present study, the above equations were recast into a one-dimensional form and discretized using the finite-difference method, which is similar to our previous work [25] using a library of PETSc [26], except for the addition of the electron energy density equation, which considers the effect of non-local electron transport. The resulting system of non-linear algebraic equations was then solved using a fully implicit backward Euler's method in the temporal domain with the Scharfetter–Gummel scheme for the mass fluxes in the spatial domain. At each time step, the resulting large sparse algebraic non-linear system was solved by a parallel fully coupled Newton–Krylov–Schwartz (NKS) algorithm, in which an additive Schwarz preconditioned GMRES is used for the solution of the Jacobian system. We have used an inexact or exact solver such as incomplete LU (ILU) or LU factorizations in each subdomain for the purpose of preconditioning. We evaluated the Jacobian matrix entries using a hybrid analytical–numerical method, in which the entries involving the derivative with respect to number density (e.g., the source terms of the species continuity equations) are expressed analytically without resorting to numerical approximation. For other entries, it can be evaluated using a standard finite-difference method. This strategy is especially useful for the plasma simulations with a large number of species and reaction channels. Details of this implementation are presented elsewhere.

"Simple" and "Complex" Helium Plasma Chemistry

For the simulation, we considered two sets of plasma chemistry (termed "simple" and "complicated"), which are summarized in Table 1 and schematically sketched in Fig. 1 for easy visualization. For the simple plasma chemistry, we considered 6 species and 10 reaction channels, which have been used frequently and successfully for RF discharge simulations. They include 6 species (e^-, He_m^*, He_2^*, He^+, He^{2+}, He) and 10 reaction channels. For the complicated plasma chemistry, we considered 7 species (e^-, He_m^*, He_{ex}^{**}, He_2^*, He^+, He_2^+, He) and 27 reaction channels, with one more species (He_{ex}^{**}) than the simple set. In general, the complicated plasma chemistry includes more reaction channels related to heavy particles, referring to Table 1, such as ion-e recombination [12], ion–electron dissociative recombination [14], ion–electron recombination [15, 16], Hornbeck–Molnar associative ionization [17], metastable-metastable associative ionization [18], metastable-induced dissociative association [22], metastable-induced association [23], dimer-induced dissociative ionization [24], dimer-induced ionization [25] and helium-atom induced dissociation [26].

The transport coefficients and the rate constants related to the electrons were calculated by solving the Boltzmann equation using BOLSIG+ [23]. Note that these coefficients were predicted and stored in a lookup table as a function of the electron temperature. The transport coefficients (mobility and diffusivity) of the ions (H^+ and He_2^+) were adopted from the experiments by Ellis et al. [24] as a function of the reduced field (E/N) and were calculated by assuming species transport in helium background gas at a temperature of 400 K. As for the diffusion coefficients of neutral species (atomic and molecular helium), they were the same as those of Yuan and Raja [12].

Table 1 Summary of simple and complicated helium plasma chemistry

No.	Reaction type	Reaction channels	Complicated*	Simple**	Threshold (eV)
00	Momentum transfer	$e + He \rightarrow e + He$	BOLSIG+	BOLSIG+	0
01	e-impact excitation	$e + He \rightarrow e + He_m^*$	BOLSIG+	$2.3 \times 10^{-16} Te^{0.31} \exp\left(\frac{-2.29 \times 10^5}{Te}\right)$	19.82*
02	e-impact excitation	$e + He \rightarrow e + He_{ex}^{**}$	BOLSIG+		22.57*
08	e-impact ionization	$e + He \rightarrow 2e + He^+$	BOLSIG+	$2.5 \times 10^{-18} Te^{0.68} \exp\left(\frac{-2.85 \times 10^5}{Te}\right)$	24.58
09	e-impact ionization	$e + He_m^* \rightarrow 2e + He^+$	BOLSIG+	$4.6 \times 10^{-16} Te^{0.6} \exp\left(\frac{-5.546 \times 10^4}{Te}\right)$	4.78
10	e-impact de-excitation	$e + He_m^* \rightarrow e + He$	2.9×10^{-15}	$1.099 \times 10^{-17} Te^{0.31}$	−19.8
11	e-impact dissociation	$e + He_2^* \rightarrow e + 2He$	3.8×10^{-15}	$1.2 \times 10^{-18} Te^{0.71} \exp\left(\frac{-3.945 \times 10^4}{Te}\right)$	−17.9
12	Ion-e recombination	$He^+ + 2e \rightarrow e + He_m^*$	6×10^{-32}	$5.38 \times 10^{-13} Te^{-0.5}$	−4.78
13	Ion-e dissociative recombination	$He_2^+ + 2e \rightarrow He_m^* + He + e$	2.8×10^{-32}		0
14	Ion-e dissociative recombination	$He_2^+ + e + He \rightarrow He_m^* + 2He$	3.5×10^{-39}		0
15	Ion-e recombination	$He_2^+ + 2e \rightarrow He_2^* + e$	1.2×10^{-33}		0
16	Ion-e recombination	$He_2^+ + e + He \rightarrow He_2^* + He$	1.5×10^{-39}		0
17	Hornbeck-Molnar associative ionization	$He_{ex}^{**} + He \rightarrow He_2^+ + e$	1.5×10^{-17}		0 ($n > 3$)
18	Metastable-metastable associative ionization	$He_m^* + He_m^* \rightarrow He_2^+ + e$	2.03×10^{-15}		−18.2
19	Metastable-metastable ionization	$He_m^* + He_m^* \rightarrow He^+ + He + e$	8.7×10^{-16}	2.7×10^{-16}	−15.8
20	Ion conversion	$He^+ + 2He \rightarrow He_2^+ + He$	6.5×10^{-44}	1.0×10^{-45}	0
21	Metastable-induced association	$He_m^* + 2He \rightarrow He_2^+ + He$	1.9×10^{-46}	1.3×10^{-45}	0
22	Metastable-induced dissociative ionization	$He_m^* + He_2^* \rightarrow He^+ + 2He + e$	5×10^{-16}		−13.5
23	Metastable-induced ionization	$He_m^* + He_2^* \rightarrow He_2^+ + He + e$	2×10^{-15}		−15.9
24	Dimer-induced dissociative ionization	$He_2^* + He_2^* \rightarrow He^+ + 3He + e$	3×10^{-16}		−11.3
25	Dimer-induced ionization	$He_2^* + He_2^* \rightarrow He_2^+ + 2He + e$	1.2×10^{-15}		−13.7
26	He-atom induced dissociation	$He_2^* + He \rightarrow 3He$	4.9×10^{-22}		0

* Martens et al. [27]

** Yuan and Raja [12]

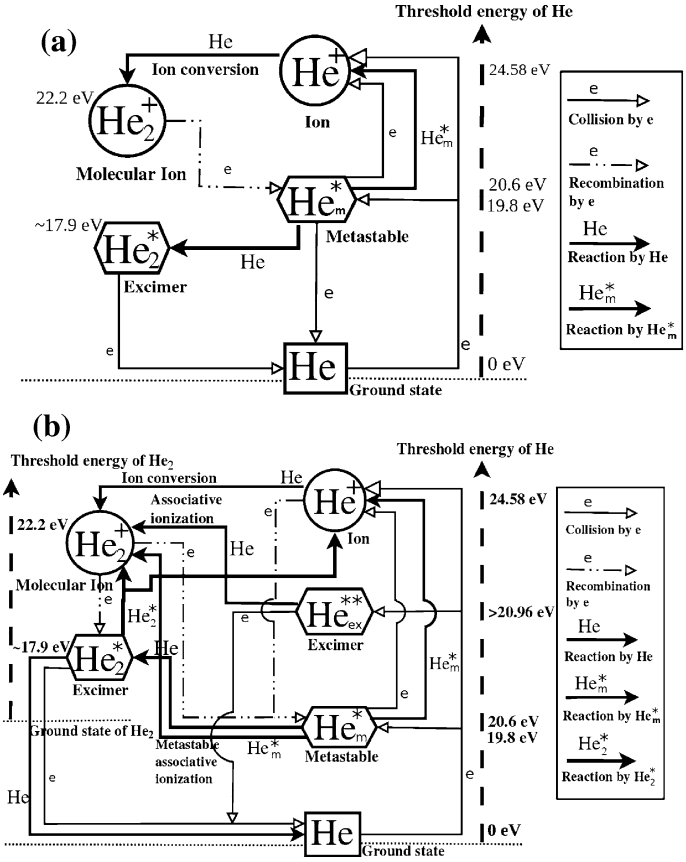

Fig. 1 Schematic diagram of **a** simple and **b** complicated helium plasma chemistry based on the magnitude of energy level

Experimental Methods

To validate directly the fluid modeling presented in the current study, we conducted corresponding experiments of helium DBD in our laboratory, which are described in detail in the following.

Figure 2 illustrates the schematic diagram of a planar atmospheric-pressure DBD along with a gas supply system and the instrumentation for electrical and OES (optical emission spectroscopy) measurements. This DBD consists of two parallel copper electrodes (50 × 50 × 8 mm each) with embedded cooling water. Each of the electrodes was covered with a 70 × 70 × 1 mm ceramic plate with measured relative permittivity of 11.63. The distance between the two dielectric plates was kept at 1 mm throughout the study. This DBD assembly was driven by a distorted-sinusoidal power supply (Model Genius-2, EN technologies Inc.) at a fixed frequency of 20 kHz. The input power from the power supply was fixed at 100 W throughout the study. The input voltage and output current waveforms across the electrodes of the parallel-plate discharge were measured by a high-voltage probe (Tektronix P6015A) and a Rogowski coil (IPC CM-100-MG, Ion Physics Corporation Inc.), respectively, through a digital oscilloscope (Tektronix TDS1012B). Helium gas

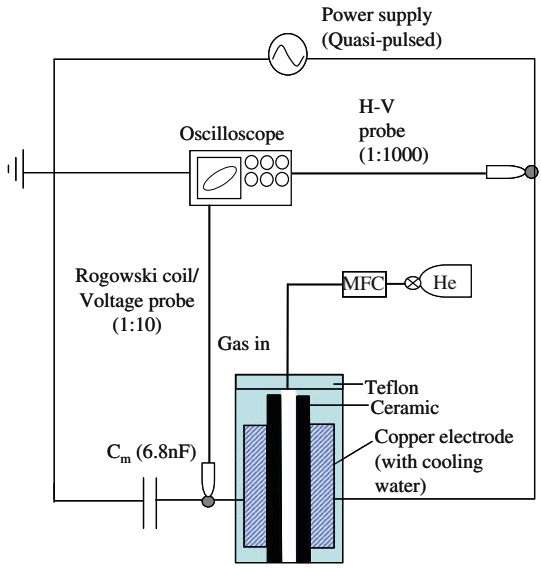

Fig. 2 Sketch of the planar helium DBD system

(99.99% purity) was used as the discharge gas that flows through the parallel plate. The flow rates were controlled by a manually adjustable flowmeter.

For comparison purposes, using the same geometrical configuration, we also produced the discharge using an RF power supply (13.56 MHz, Dressler HF-Technik GmbH, Cesar 1310) connected to a matching box (Dressler HF-Technik GmbH, VM 1000 A/AW). The input power from the power supply was fixed at 12 W. The input voltage and output current waveforms across the electrodes of the parallel-plate discharge were measured by a current probe (Tektronix TCP312) and a high-voltage probe (Tektronix P6015A) through a digital oscilloscope (Tektronix TDS1012B).

Results and Discussion

Comparison of the Discharged Current Between the Simulation and the Experiment

The input voltage waveform for the simulations was obtained by Fourier series expansion of the measured voltage waveform across the electrodes using 50 terms of sine and cosine functions with 20 kHz as the fundamental frequency. In general, this fitting method can be applied to any arbitrary realistic voltage waveform. The simulated temporal discharge currents along with the measurements are presented in Fig. 3. Note that the powered electrode is placed at $x = 0$ mm while the grounded electrode is placed at $x = 3$ mm throughout the current study. The results show that the predicted temporal currents using the complex plasma chemistry are in excellent agreement with the measurements, while those using the simple plasma chemistry fail to reproduce the measurements during some periods in a cycle. These regions of discrepancy include over-prediction of major discharge current peaks and under-prediction between major current peaks. This implies that the inclusion of the more excited helium, metastable helium and electron–ion-related detailed reaction channels is responsible for the successful fluid modeling of the helium AC DBD, which is different from the simulation of the helium RF discharge under the atmospheric-pressure

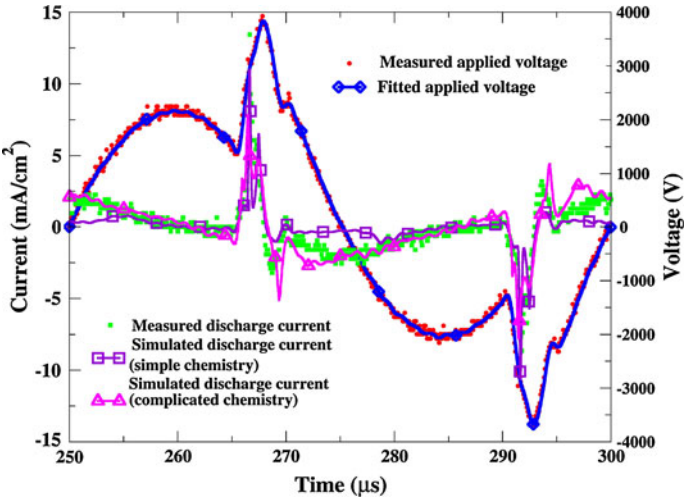

Fig. 3 Comparison of simulated and measured discharge currents in a distorted-sinusoidal AC cycle (20 kHz)

condition. Note that the application of the simple plasma chemistry was able to reproduce the experimental data as well as the complex plasma chemistry under similar geometry (1 mm gap with 1 mm ceramic dielectrics each side), as presented in Fig. 4a. Figure 4b shows that, in the helium RF discharge, most of the electrical power input is absorbed by the electrons in the plasma bulk region, similar to the low-pressure condition, since the oscillating frequency of the voltage is very fast and most of the electrons are unable to drift to the dielectric surfaces in such a short period of time before the applied voltage changes direction. However, in the helium AC DBD, it is a typical Townsend-like discharge most of the time during a cycle period (maximal current density ~ 8 mA/cm^2 in Fig. 3 and $n_e << n_{He_2^+}$, which will be shown later), because most of the electrons are able to drift in time towards the dielectric surfaces with a small gap (1 mm) during a half cycle. This makes most of the electrical power be absorbed by the ions (He_2^+), rather than by the electrons as in the helium RF case.

As a brief summary, the present fluid modeling code using the complex plasma chemistry can predict quantitatively the temporal evolution of the discharged current of helium DBD driven by a 20 kHz distorted-sinusoidal power source very well, which is rarely reported in the literature. In addition, our study shows that the use of LMEA can produce very faithful simulation results of DBD, as compared with the experimental data, because of the consideration of the non-local effect of electron energy distribution and inclusion of electron-neutral elastic collision effect, which are especially important in APPs. This quantitative validation provides us with confidence in interpreting the discharge physics of helium DBD based on the simulations using the complex plasma chemistry, which are presented next.

Spatial Profiles of Cycle-Averaged Plasma Properties

Figure 5 shows the cycle-average spatial power absorption by the plasma through various mechanisms. It shows that the molecular ions (He_2^+) absorb much more power through

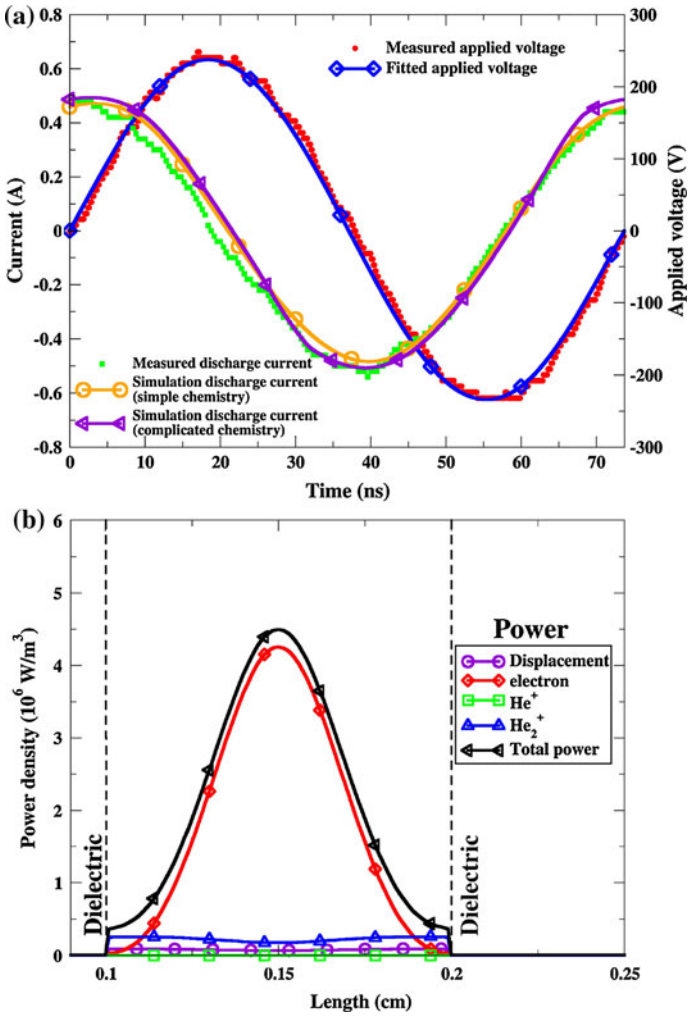

Fig. 4 **a** Comparison between experimental current and simulation for an atmospheric-pressure RF discharge using the simple plasma chemistry. **b** Power absorption by various mechanisms using the simple helium chemistry

ohmic heating than the electrons do near both the dielectric surfaces, which is caused by the much higher concentration of the molecular ions than that of the electrons ($\sim$ 1 order), as can be seen clearly in Fig. 6. Figure 6 illustrates the cycle-average spatial distribution of various plasma properties. It shows that the cycle-average number density of He_2^+ is much higher than that of the electrons ($\sim$1 order) and He^+ (2–3 orders), which leads to the observation that the power absorption by the electrons and He^+ is small and essentially negligible, respectively. This also confirms that it is a typical Townsend discharge in the average sense: many more ions exist than electrons. This conclusion was also obtained by the early high-pressure helium experiments [28]. The abundant He_2^+ is formed through the ion conversion channel ($He^+ + 2He \rightarrow He_2^+ + He$), which was first found by Phelps and Brown [29]. The average electron temperature is nearly uniform across the gap and is as

high as 5.4 eV. The two most populated neutral species are metastable He_m^* and excimer He_2^* (or $He_2^* > He_m^* > > He_{ex}^{**}$), mainly due to a series of ion–electron recombination, in addition to the direct electron-impact excitation, as shown in Table 1.

Temporal Variation of Spatial-Average Plasma Properties

Figure 7 shows the temporal variation of the power dissipation through various mechanisms similar to those presented in Fig. 5 for the RF case. Again, it shows that molecular helium ions dissipate most of the electrical power input by the distorted-sinusoidal power source at any instant during a typical cycle, especially during several breakdown periods (higher power density). Also, the power dissipation by other mechanisms such as atomic helium ions is negligible.

Figure 8 shows a series of temporal variations of several important discharge properties in a cycle using the complex chemistry, which include: (a) the applied voltage, discharge current, dielectric voltage, gap voltage and accumulated charge densities on both powered and grounded dielectrics, (b) the spatial-average concentrations of charged particles and electron temperature and (c) the spatial-average concentrations of excited, metastable non-charged heavy particles. We divided the first half cycle (the rising voltage period) into several distinct modes of discharge, which include long Townsend-like discharge (region A), dark-current-like discharge (region B), primary short Townsend-like discharge (region C) and secondary short Townsend-like discharge (region D), for the convenience of discussion as described next.

Figure 8a shows that the gap voltage has a very strong "memory effect" because of the shielding caused by the accumulated charges on the dielectric surfaces. The discharge current correlates very well with the gap voltage, which is shielded by the accumulated charges on the dielectric surfaces. Also, the dielectric voltage is almost the same across both dielectrics, of which we have plotted only one for clarity. It is also clear that the

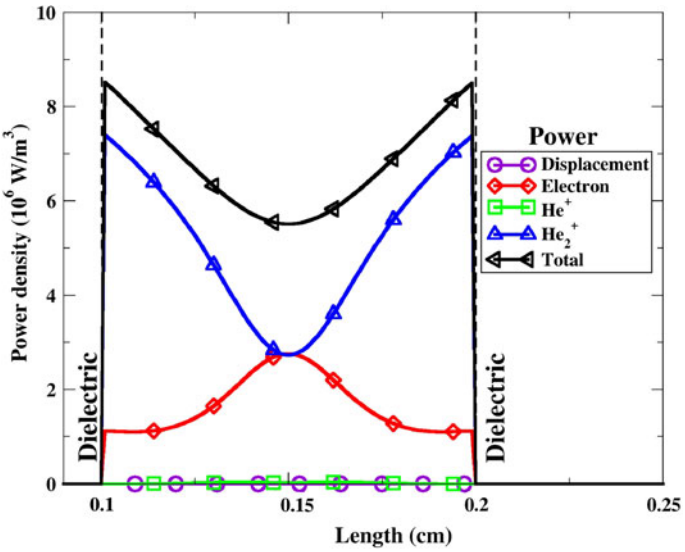

Fig. 5 Time-averaged spatial power absorption by various mechanisms for the atmospheric-pressure helium DBD driven by a distorted-sinusoidal power source (20 kHz)

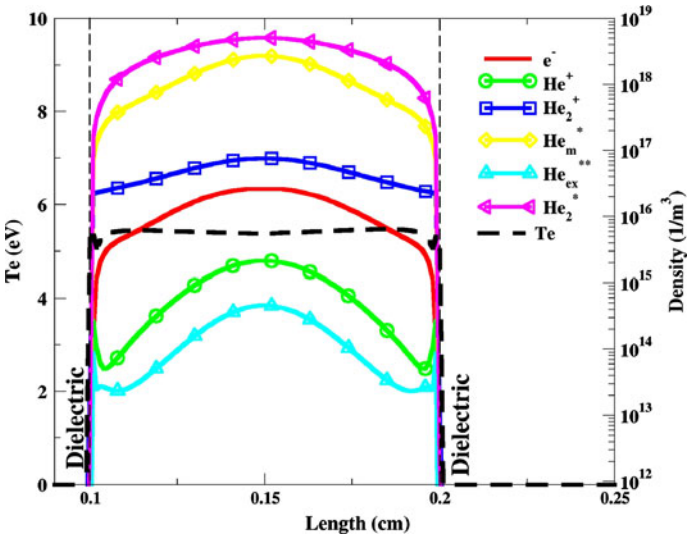

Fig. 6 Spatial profiles of cycle-averaged discharge properties for the atmospheric-pressure helium DBD driven by a distorted-sinusoidal power source (20 kHz)

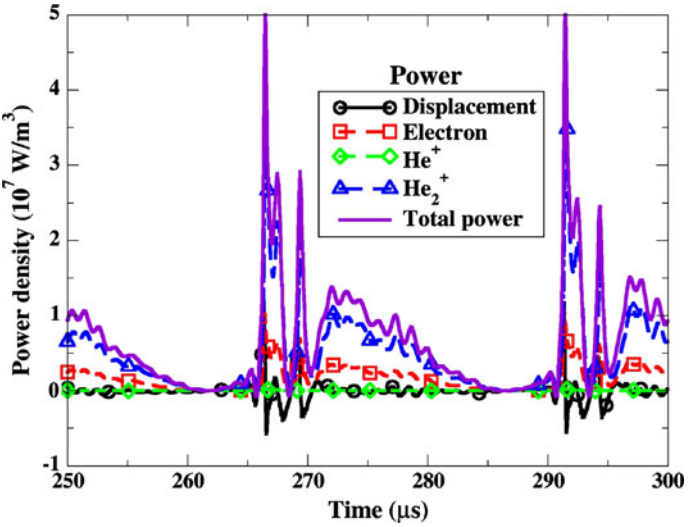

Fig. 7 Temporal variation of spatial-averaged power absorption by electrons and molecular helium ions by using the complex chemistry for the helium DBD driven by a 20 kHz distorted-sinusoidal power supply

temporal variation in the accumulated charges on the grounded dielectrics correlates very well with the change in dielectric voltage. This is attributed to the linearity of the electrostatic Poisson equation. The surface charges at the dielectric surface of the ground electrode contribute to the volumetric charge density (a source term of the Poisson equation) and thus influence the potential distribution near the interface in a linear fashion. Interestingly, the accumulated charges on both dielectric surfaces are nearly the same in

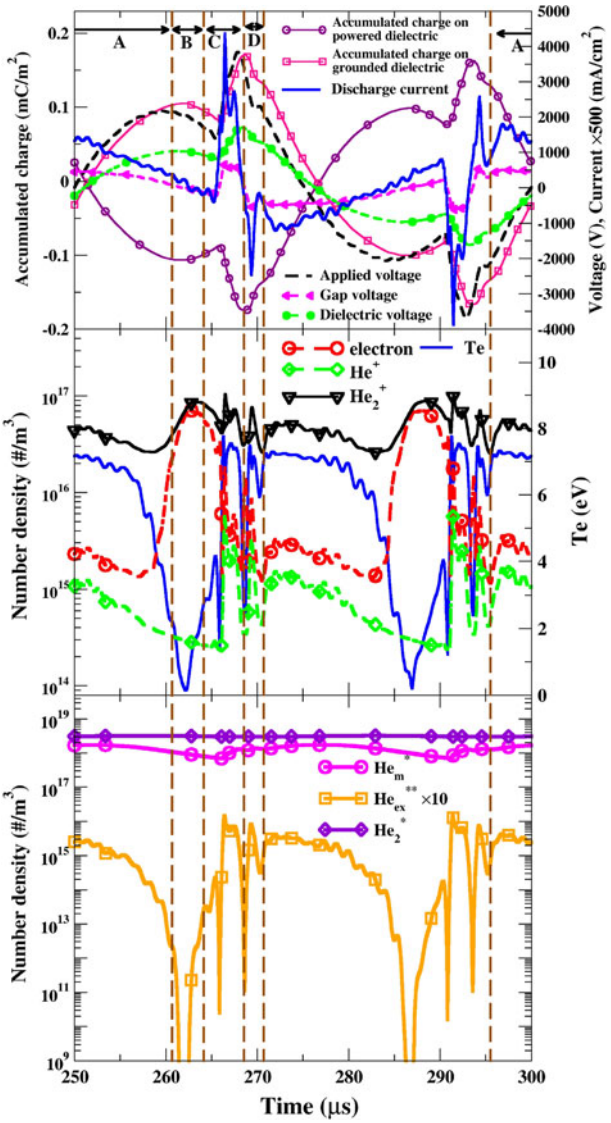

Fig. 8 Temporal variation of spatial-averaged plasma properties for the atmospheric-pressure helium DBD driven by a distorted-sinusoidal power source (20 kHz)

magnitude but opposite in sign. This is attributed to the discharge being a Townsend-like breakdown (very few electrons compared with ions) most of the time during a cycle, in which the electric field across the gap is not distorted, which makes the system act like a standard capacitor.

Figure 8b shows that the molecular helium ions (3×10^{16}–10^{17} m^{-3}) are the most dominant species almost at any instant (regions A, C and D), instead of the atomic helium ions, except in the early stage of region B, where there is approximately the same amount of electrons as the sum of molecular and atomic helium ions. This is attributed to the

pronounced Hornbeck–Molnar associative ionization ($He_{ex}^{**} + He \rightarrow He_2^+ + e$) (No. 17 in Table 1). In regions A, C and D, they are all typical Townsend-like discharges, in which many more ions exist than electrons (~2 orders of magnitude larger). Although the number of electrons is small, the electron temperatures are observed to be relatively high, in the order of 7 eV, except in region B and the early stage of region C. In addition, region B is termed a "dark-current-like" region because of the quasi-neutrality in the plasma bulk, the very low discharge current ($\ll$1 mA/cm^2) and the very low electron temperature.

The spatial-average concentrations of several important heavy non-charged species are presented in Fig. 8c. The results show that both the excimer helium (He_2^*, most abundant) and the metastable helium (He_m^*) are the most dominating neutral species at all times during a cycle, while there is much less excited helium (He_{ex}^{**}) (>4 order of magnitude) with an almost vanishing value in region B (dark-current-like) where the electron temperature is nearly negligible in the bulk, which is not able to excite the helium from the ground state.

In the following, the typical detailed distribution of the discharge properties in each region will be presented next to elucidate the underlying physics.

Region A: Long Townsend-Like Region

In this region A, the gap voltage decreases with time because of the memory effect, as mentioned earlier (shielded by increasing negative and positive accumulated charges at powered and grounded dielectrics, respectively), although the applied voltage increases with time, as shown in Fig. 8a. The magnitude of the maximum current density is ~2.4 mA/cm^2, which is a typical characteristic of Townsend-like discharge, and the temporal width is ~15 μs in region A. It is termed "long" because it lasts for 15 μs for a cycle period of 50 μs. The typical snapshots of plasma properties are shown in Fig. 9 as the applied voltage reaches 1,150 V. At this instant, the electrons and ions are attracted to the anode and cathode, respectively, and the average electron temperature is as high as 7 eV

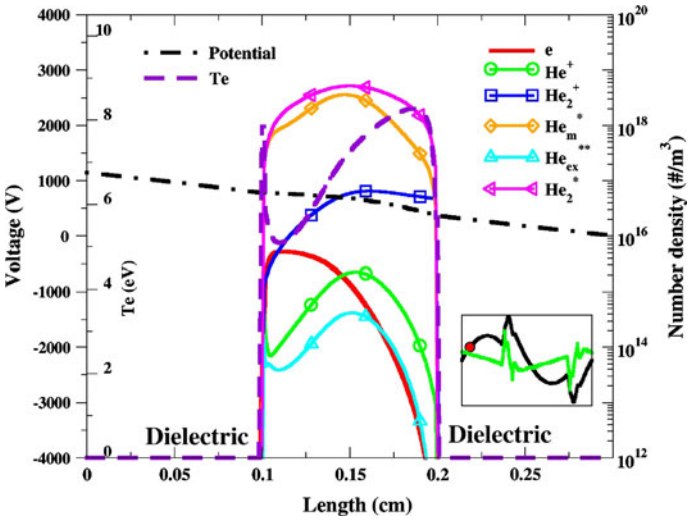

Fig. 9 Snapshots of distribution of typical plasma properties in region A (long Townsend like at V ~1,150 volts) of a helium DBD driven by a distorted-sinusoidal power source (20 kHz)

(Fig. 8b). In general, the electron density is far lower than the molecular helium ion density across the gap, except in the small region near the anode, which is a typical characteristic of a Townsend-like discharge. The generation of the Townsend-like discharge is attributed to a larger electric field in the right-hand half of the gap, very light electrons and a very narrow gap (1 mm), which make the electrons move to the cathode within a very short period. Similar to those presented in Fig. 6 for the cycle-averaged data, the number densities of excimer (He_2^*) and metastable (He_m^*) helium are the most dominant species in the range of 10^{18}–10^{19} m^{-3}, which are 2 and 3–5 orders of magnitude larger than the number density of molecular helium ions (10^{17} m^{-3}) and electrons, respectively. However, the excited atomic helium (He_{ex}^{**}) is much smaller and in the order of 10^{14} m^{-3}. Note that the lifetime of the excited atomic helium is very short and is easily de-excited, which can emit visible fluorescence. Correct prediction of the discharge current using the complex plasma chemistry in region A is attributed to the inclusion of channels like Hornbeck–Molnar associative ionization (No. 17 in Table 1), metastable-metastable associative ionization (No. 18 in Table 1) and several dimmer- and metastable-related ionization channels (Nos. 21, 23 and 25 in Table 1), which can generate abundant molecular helium ions for producing enough discharge current as compared with the simple plasma chemistry. Thus, the use of complex plasma chemistry by including more heavy-particle-related channels in the fluid modeling as mentioned above can faithfully reproduce the experimental discharge current in region A.

Region B: Dark-Current-Like Discharge

In region B, the gap voltage decreases with decreasing applied voltage and the current density becomes very small (maximal value $\ll$ 1 mA/cm^2), which is much smaller than the current in the previous long Townsend-like discharge (Fig. 8a). In addition, the magnitude of accumulated charges on both dielectrics begins to decrease gradually, which leads to a slightly decreased dielectric voltage (Fig. 8a). This region lasts for only $\sim$3.5 μs. Typical snapshots of plasma properties are shown in Fig. 10 as the applied voltage reaches $\sim$2,000 V, at which the gap voltage changes from positive to negative and the magnitudes of the accumulated charges on both dielectric surfaces reach their maximum values. At this instant, a clear quasi-neutral plasma bulk region with very high plasma density in the order of 10^{17} m^{-3} with a width of $\sim$0.5 mm is formed in the center of the gap; however, the electron temperature becomes very low, except near the sheath ($\sim$2 eV). The sheath potential (thus the electric field) is very small because of the almost vanishing gap voltage at this instant. The electrons in the sheath are thus not accelerated to gain energy. This leads to the disappearance of short-lived excited helium (He_{ex}^{**}), which requires energetic electrons to "pump up" its population at higher energy states (Fig. 10). However, the metastable and excimer heliums are still as abundant as those in region A because they are relatively long-lived compared with the He_{ex}^{**}. Nevertheless, the abundant electrons generated by those previously mentioned ionization channels (in region A) can still be kept inside the gap because of this very small electric field and form the quasi-neutral plasma bulk. After this instant, the electric field begins to increase with increasingly negative gap voltage (Fig. 8a), which leads to the increase in electron temperature, as can be seen from Fig. 8b.

By summing up the above observations, we can conclude that it is a "dark-current-like", instead of a glow-like, discharge in region B because of the very small discharge current, the very small amount of short-lived excited helium and the very low electron

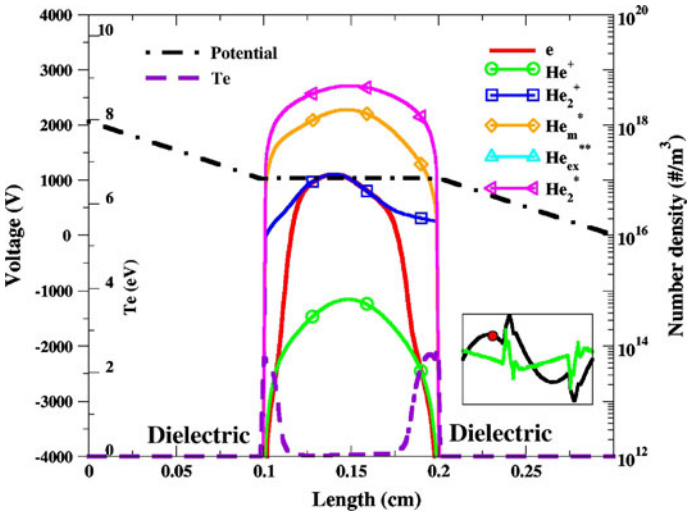

Fig. 10 Snapshots of distribution of typical plasma properties in region B (dark current like at V ~2,000 volts) of helium DBD driven by a distorted-sinusoidal power source (20 kHz)

temperature, although abundant charged species with quasi-neutrality plasma bulk still exist in the gap.

Region C: Primary Short Townsend-Like Discharge

In region C, the gap voltage increases rapidly initially from −250 V up to ~750 V and remains at this voltage for a period of ~2 μs because the shielding from increasing accumulated charges on dielectric surfaces balances with the increasing applied voltage (Fig. 8a). The magnitude of the maximal discharge current is about ~8 mA/cm^2 and the electron density is much lower than the ion density (especially the molecular ion), while the electron temperature is relatively high (~7 eV on average) (Fig. 8b). Typical snapshots of plasma properties are shown in Fig. 11 as the applied voltage is at ~3,000 V, at which the discharge current peaks. The discharge phenomena are very similar to those described in region A, that is, a Townsend-like discharge; however, this is termed "primary short" because the period of the discharge is shorter (3–4 μs) and the discharge current is much larger. This short and large discharge current is mainly caused by the very large rate of increase of the applied voltage (pulse; from ~1,500 to ~3,000 V in less than 1 μs), which in turn causes the gap voltage to increase in a similar fashion. This rapid increase in the voltage attracts a large amount of electrons and molecular ions to move very quickly towards the anode and cathode, respectively (Fig. 8a). This in turn quickly shields the applied voltage and then after this short current peak the gap voltage remains at an approximately constant value because the shielding caused by the charge accumulation on both dielectrics cancels out the increase in applied voltage.

Region D: Secondary Short Townsend-Like Discharge

In region D, a secondary short Townsend-like discharge (~1–2 μs) is induced as the applied voltage rapidly decreases from ~3,500 down to ~2,400 V within 1 μs (the gap

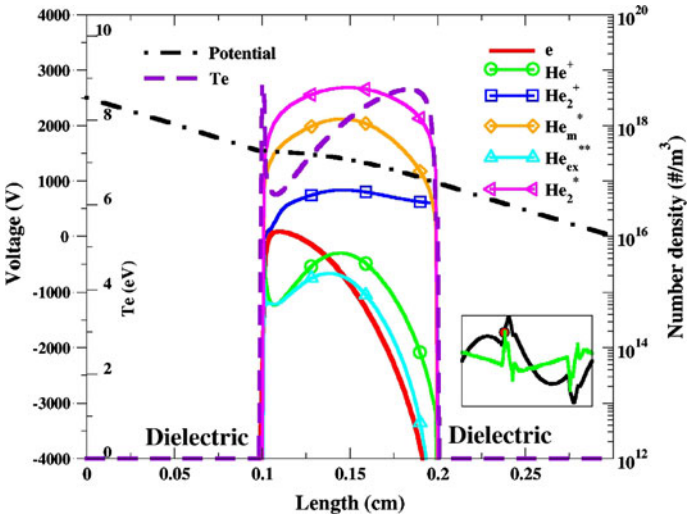

Fig. 11 Snapshots of distribution of typical plasma properties in region C (primary short Townsend like at V ~3,000 volts) of a helium DBD driven by a distorted-sinusoidal power source (20 kHz)

voltage reverses from 500 to −500 V), which was also experimentally observed by Chiper et al. [30]. The corresponding maximal current density is ~5 mA/cm^2. Because of the polarity change in the gap voltage the electrons and ions rapidly accumulate on the grounded (anode) and powered (cathode) dielectric surfaces, respectively, which reduces the magnitude of the surface charges on both dielectric surfaces simultaneously, as shown in Fig. 8a. This in turn reduces the dielectric voltage. In other words, this short secondary Townsend-like discharge is formed due to the rapid gap voltage reversing. The snapshots of typical plasma properties are shown in Fig. 12 as the applied voltage is at ~2,300 volts, at which the negative discharge current peaks. Again, these data show that it is a typical Townsend-like discharge.

Phase Diagram of Discharge Properties

To elucidate better and have an overview of the helium DBD driven by the distorted-sinusoidal power source, we next present spatial–temporal phase diagrams of several important discharge properties. Figures 13, 14 and 15 illustrate the phase diagram of the electron density, He_2^+ density and electron temperature distribution, respectively, along with the vertically placed temporal simulated discharge current in the center for better visualization. As can be seen, in the long Townsend-like discharge region (region A), most of the electrons are attracted to the anode (powered), while the He_2^+ mainly prevails in most of the region across the gap, especially close to the cathode (grounded). Also, the ions outnumber the electrons across the gap, except in the region very close to the anode. The electron temperatures are generally very high, in the order of 7–8 eV close to the cathode side. In the dark-current-like region (region B), the distributions of the electrons and He_2^+ are very similar, and form a quasi-neutral zone in the center. This quasi-neutral zone moves from the anode side (powered) towards the cathode side (grounded) at a slow speed of ~100 m/s. At the same time, the electron temperatures are nearly zero in the most central part of the gap, except the narrow regions very close to the two dielectric surfaces. This

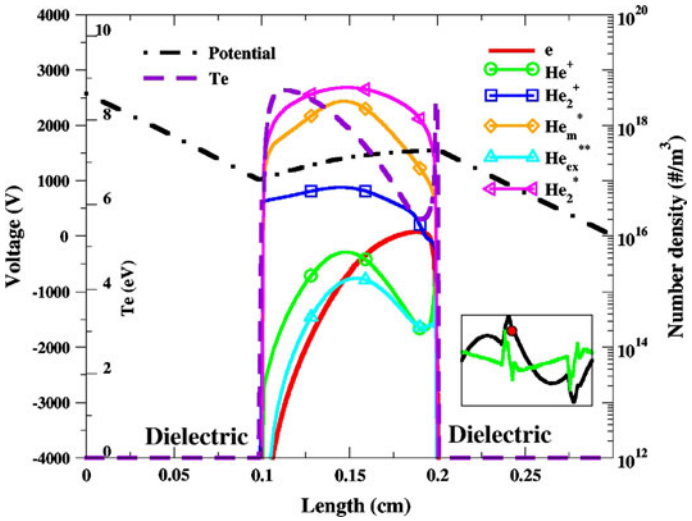

Fig. 12 Snapshots of distribution of **a** plasma properties in region D (Secondary short Townsend like discharge at V ~2,300 volts) of a helium DBD driven by a distorted-sinusoidal power source (20 kHz)

results in the rapid disappearance of excited atomic helium (He_{ex}^{**}) (shown in Figs. 8c, 10) and thus almost no fluorescence is emitted. Thus, we term this region the "dark-current-like" region. After the dark-current region, i.e., in the primary short Townsend-like discharge (region C), similar to region A, the electrons move to the region close to the anode side (powered), while the ions move to the cathode side (grounded) with a much higher concentration than in region A. Also, the electron temperatures are much higher in the region close to the cathode, in the range of 8–10 eV, caused by the very large electric field in that region. In region D, the secondary short Townsend-like discharge region, the electrons move to the cathode side (powered) while the ions move to the anode side (grounded), since the voltage (and the current) is reversed compared with that in regions A and C. The electron temperatures are also high close to the powered electrode side (anode). After this region, the discharge repeats the regions A–D, but with the opposite polarity because of the reversed applied voltage. One interesting thing to notice in Fig. 15 is that there are two very short regions (less than 0.3 μs; in the early stage of region C and between regions C and D), in which the electron temperatures are nearly zero across the gap, except the regions close to the dielectrics. In these two regions, all the data show that they are also typical "dark-current-like" discharges as described above, although they are very short in time.

Conclusion

In the present study, we have investigated in detail the non-equilibrium atmospheric-pressure helium dielectric barrier discharge driven by a realistic distorted-sinusoidal voltage power source (20 kHz) using a self-consistent one-dimensional fluid modeling code using LMEA. Two sets of helium plasma chemistry that are often found in the literature were used to model the helium DBD. The simulated temporal discharged currents using the complex plasma chemistry are in excellent agreement with the measurements

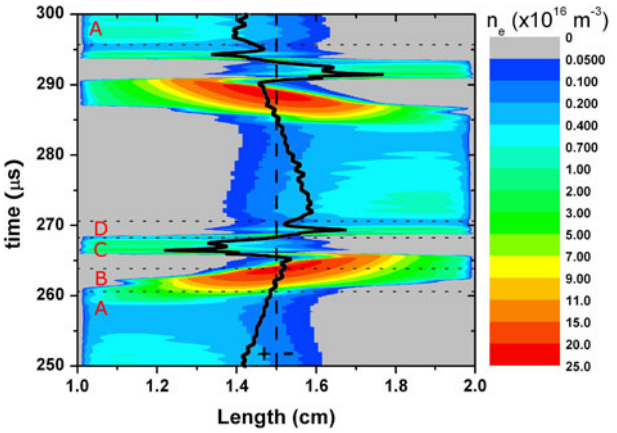

Fig. 13 Phase diagram of electron number density distribution of a helium DBD driven by a distorted-sinusoidal power source (20 kHz)

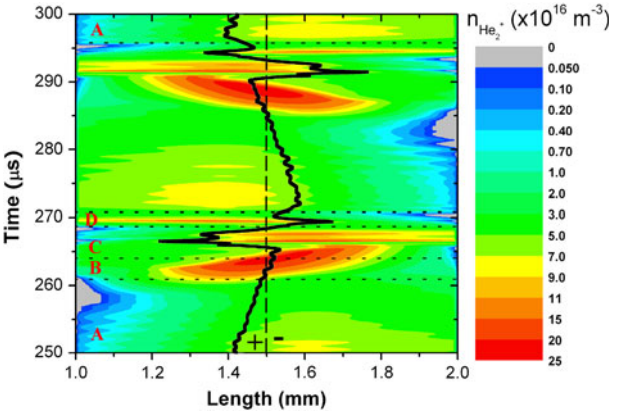

Fig. 14 Phase diagram of He_2^+ number density distribution of a helium DBD driven by a distorted-sinusoidal power source (20 kHz)

obtained in the present study, which validates the fluid present modeling code. This observation should be attributed to two factors: (1) the use of LMEA in our fluid modeling, which considers the non-local electron energy transport, instead of LFA like others, and the inclusion of electron-neutral elastic collision effect, which are especially important in the APPs and (2) the inclusion of heavy-particle-related and electron–ion-related reactions in the complex plasma chemistry, which is critical for accurately predicting the helium DBD because of the slow varying electric field in the range of tens of kilohertz. Based on the simulations, the helium DBD with a gap of 1 mm in width shows several interesting mode transitions, which can be classified sequentially into long secondary Townsend-like (region A), dark current-like (region B), short primary Townsend-like (region C) and short secondary Townsend-like (region D) discharges, based on the predicted discharged properties. In addition, the externally supplied electrical power is absorbed mostly by the molecular helium ions at the driving frequency of 20 kHz, rather than by the electrons as in an RF

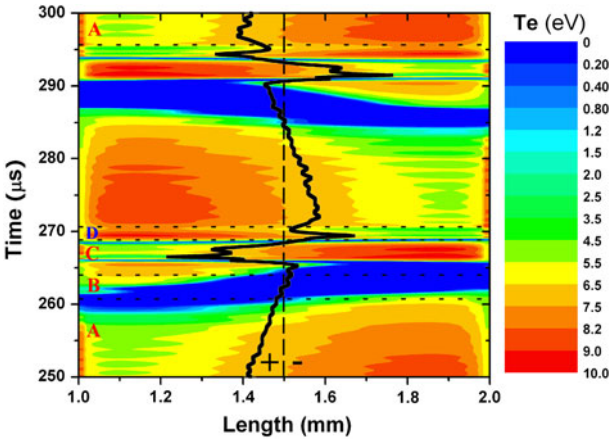

Fig. 15 Phase diagram of electron temperature distribution of a helium DBD driven by a distorted-sinusoidal power source (20 kHz)

discharge. Further studies varying the frequency, gap distance, dielectric thickness and dielectric material for helium DBD with oxygen addition driven by a distorted-sinusoidal voltage AC power source are currently in progress and will be reported in the very near future.

Acknowledgments The authors would like to thank the financial support by the National Science Council of Taiwan (NSC 96-2628-E-009-134-MY3), ITRI/MCL through Dr. Bee-Yu Wei, Institute of Nuclear Energy Research (992001INER028) and Ministry of Economic Affairs of Taiwan.

References

1. Iwasaki M, Matsudaira Y, Takeda K, Ito M, Miyamoto E, Yara T, Uehara T, Hori M (2008) J Appl Phys 103:023303
2. Borcia G, Chiper A, Rusu I (2006) Plasma Sources Sci Technol 15:849–857
3. Morent R, De Geyter N, Jacobs T, Van Vlierberghs S, Dubruel P, Leys C, Schacht E (2009) Plasmas Process Polym 6:S537–S542
4. Park JB, Kyung SJ, Yeom GY (2008) J Appl Phys 104:083302
5. Thiyagarajan M, Alexeff I, Parameswaran S, Beebe S (2005) IEEE Trans Plasma Sci 33:322–323
6. Takaki K, Hatanaka Y, Arima K, Mukaigawa S, Fujiwara T (2008) Vacuum 83:128–132
7. Okubo M, Yoshida K, Yamamoto T (2008) IEEE Trans Ind Appl 44:1410–1417
8. Kogelschatz U, Eliasson B, Egli W (1999) Pure Appl Chem 71:1819–1828
9. Serafetinides AA, Tsikrikas GN, Atanasov PA (1998) Opt Laser Technol 30:159–162
10. Park J, Henins I, Herrmann HW, Selwyn GS (2001) J Appl Phys 89:20
11. Yuan X, Raja LL (2002) Appl Phys Lett 81:814
12. Yuan X, Raja LL (2003) IEEE Trans Plasma Sci 31:495
13. Shang W, Wang D, Zhang Y (2008) Phys Plasma 15:093503
14. Chirokov A, Khot SN, Gangoli SP, Fridman A, Henderson P (2009) Plasma Source Sci T 18:025025
15. Massines F, Rabehi A, Decomps P, Gadri RB, Segur P, Mayoux C (1998) J Appl Phys 83:2950
16. Tochikubo F, Chiba T, Watanabe T (1999) Jpn J Appl Phys 38:5244
17. Mangolini L, Anderson C, Heberlein J, Kortshagen U (2004) J Phys D Appl Phys 37:1021
18. Golubovskii YB, Maiorov VA, Behnke J, Behnke JF (2003) J Phys D Appl Phys 36:39
19. Wang D, Wang Y, Liu C (2006) Thin Solid Films 506–507:384–388
20. Bartnikas R, Radu I, Wertheimer MR (2007) IEEE Trans Plasma Sci 35:1437
21. Wang Q, Sun J, Wang D (2009) Phys Plasma 16:043503

22. Grubert GK, Becker MM, Loffhagen D (2009) Phys Rev E 80:036405
23. BOLSIG. http://www.siglo-kinema.com/bolsig.htm
24. Ellis HW, Pai RY, McDaniel EW, Mason EA, Viehland LA (1976) Atomic Data Nucl Data Tables 17:177–180
25. Hung CT, Hu MH, Wu JS, Hwang FN (2007) Comput Phys Commun 177:138–139
26. Balay S, Buschelman K, Gropp WD, Kaushik D, Knepley MG, McInnes LC, Smith BF, Zhang H (2009) http://www.mcs.anl.gov/petsc
27. Martens T, Bogaerts A, Brok W (2007) Anal Bioanal Chem 388:1583–1594
28. Deloche R, Monchicourt P, Cheret M, Lambert F (1976) Phys Rev A 13:1140
29. Phelps AV, Brown SC (1952) Phys Rev 86:102
30. Chiper AS, Cazan R, Popa G (2008) IEEE Trans Plasma Sci 36:2824